Solid State Ionics 413 (2024) 116620

Contents lists available at ScienceDirect

Solid State Ionics

journal homepage: www.elsevier.com/locate/ssi

Impact of the electrospinning synthesis route on the structural and electrocatalytic features of the LSCF ($La_{0.6}Sr_{0.4}Co_{0.2}Fe_{0.8}O_{3-\delta}$) perovskite for application in solid oxide fuel cells

Marta Daga [a], Caterina Sanna [a], Giorgio Bais [b], Maurizio Polentarutti [b], Sara Massardo [e,2], Marilena Carnasciali [a], Peter Holtappels [c,1], Paola Costamagna [a,*], Marcella Pani [a,d,*], Cristina Artini [a,e]

[a] DCCI, Department of Chemistry and Industrial Chemistry, University of Genoa, Via Dodecaneso 31, I-16146 Genoa, Italy
[b] Elettra- Synchrotron Trieste, ss14, km 163.5, Basovizza, 34149 Trieste, Italy
[c] DTU Energy, Technical University of Denmark, Elektrovej 375, DK-2800 Kgs. Lyngby, Denmark
[d] CNR-SPIN, Italian National Research Council, Corso Perrone 24, 16152 Genoa, Italy
[e] CNR-ICMATE, Italian National Research Council, Via De Marini 6, 16149 Genoa, Italy

ARTICLE INFO

Keywords:
Materials science
Energy materials
Mixed conductors
Electrochemistry
Solid oxide fuel cells

ABSTRACT

In-house electrospun $La_{0.6}Sr_{0.4}Co_{0.2}Fe_{0.8}O_{3-\delta}$ (LSCF) nanofibers have been tested through synchrotron x-ray diffraction and electrochemical impedance spectroscopy (EIS) in the 823–1173 K range, namely in the operating window of intermediate-temperature solid oxide fuel cells. Identical tests have been carried out on commercial LSCF powders, as a control sample. The results demonstrate that the electrospinning manufacturing procedure influences the crystalline properties of the perovskite. The rhombohedral structure (R), stable at room temperature, is retained by nanofibers throughout the whole temperature range, while a rhombohedral to cubic transition (R→C) is detected in powders at ~1023 K as a discontinuity in the rhombohedral angle α, accompanied by an abrupt change in oxygen occupation and microstrain. EIS data have a single trend in the nanofibers Arrhenius plot, and two different ones in powders, separated by a discontinuity at the structural transition temperature. Thus, a striking parallel is demonstrated between the variation with temperature of crystallographic features and electrochemical performance. Interestingly, this parallel is found for both nanofiber and granular electrodes. This opens up questions and new perspectives in attributing activation energies derived from EIS tests of LSCF materials to electrochemical processes and/or crystal structure variations.

1. Introduction

The employment of intermediate temperature-solid oxide fuel cells (IT-SOFCs) operating between 873 and 1073 K offers indisputable advantages, such as enhanced cell lifespan, but also drawbacks, mainly associated with the lowering of the cell performance. To overcome this problem, many efforts of the scientific community focus on identifying high-performance electrolytes and electrodes. Among the latter, mixed ionic-electronic conductors (MIECs) [1] are favored, due to their two-fold role, with perovskite-based oxides being particularly interesting materials for IT-SOFC cathodes [2–7]. Among perovskites, the $La_{1-x}Sr_xCo_{1-y}Fe_yO_{3-\delta}$ system is the most promising one thanks to its superior catalytic activity toward the oxygen reduction reaction (ORR) [8], and $La_{0.6}Sr_{0.4}Co_{0.2}Fe_{0.8}O_{3-\delta}$ (LSCF) is one of the most commonly employed compositions in IT-SOFCs [8].

Perovskites are extremely flexible in accommodating a large number of different ions in their structure, which has a high tolerance toward distortions and non-stoichiometry [9]. These compounds are characterized by general formula ABO_3, and in the ideal case by a cubic cell (C, $Pm\bar{3}m$ space group), where the bigger cation A and the smaller B are

* Corresponding authors at: DCCI, Department of Chemistry and Industrial Chemistry, University of Genoa, Via Dodecaneso 31, I-16146 Genoa, Italy.
E-mail addresses: paola.costamagna@unige.it (P. Costamagna), marcella.pani@unige.it (M. Pani).
[1] Present address: Karlsruhe Institute of Technology (KIT), Institute for Micro Process Engineering (IMVT), Hermann-von-Helmholtz-Platz 1, D-76344 Eggenstein-Leopoldshafen, Germany.
[2] The work was conducted when the affiliation was with DCCI.

https://doi.org/10.1016/j.ssi.2024.116620
Received 22 March 2024; Received in revised form 22 May 2024; Accepted 8 June 2024
Available online 17 June 2024

respectively in 12-fold and octahedral coordination with oxygen ions, correspondingly occupying the 1*b* site at (1/2,1/2,1/2) and the 1*a* site at (0,0,0); oxygen is in 3*d* at (1/2, 0, 0). However, the majority of perovskites exhibit a structural distortion deriving from the tilting of BO_6 octahedra, thus assuming one of the 23 theoretically possible configurations, as described by Glazer [10] and Aleksandrov [11] in 1970s.

The crystal structure of perovskites is finely tuned by temperature and composition: in $La_{1-x}Sr_xCo_{1-y}Fe_yO_{3-\delta}$, where La and Sr share the A-site, and Co and Fe occupy the B-site, the transition from the rhombohedral (R, $R\bar{3}c$ space group) to the cubic C crystal system is observed when $x \geq \sim 0.6$ [12]; conversely, if $x = 0.4$, $La_{0.6}Sr_{0.4}Co_{0.2}Fe_{0.8}O_{3-\delta}$ crystallizes in the R form at room temperature, and transforms into C at high temperature, following a second-order law [13]. It is noteworthy that R is one of the 9 experimentally observed perovskites distortions, and one of the two most commonly encountered ones, out of the 23 predicted [10]. The R → C transition is common to all the compositions of the $La_{1-x}Sr_xCo_{1-y}Fe_yO_{3-\delta}$ system, but the exact temperature at which it occurs depends on the oxide stoichiometry. For instance, a study on $La_{0.6}Sr_{0.4}Co_{0.8}Fe_{0.2}O_{3-\delta}$ [14], located the R → C transition between 673 and 773 K, while the same transition occurs between 973 and 1073 K in $La_{0.6}Sr_{0.4}Co_{0.2}Fe_{0.8}O_{3-\delta}$ [13,15], and at 1073 K in $La_{0.6}Sr_{0.4}FeO_{3-\delta}$ [16]. These significant discrepancies most probably deal with the Fe/Co content ratio: the larger bonding energy associated with Fe—O when compared to Co—O is the reason behind the higher transition temperature in Fe-rich compositions [17]. Notably, identifying the R → C transition *via* x-ray diffraction is quite challenging, due to peaks overlap between the two phases.

A common strategy to enhance electrode performance involves doping it with electrolyte materials like Gd- or Sm-doped, *via* different methods, such as infiltration [18,19], core-shell nanocomposites preparation [20] or co-electrospinning [21]. This approach has a twofold purpose: (1) to increase the electrode's ionic conductivity while extending the three-phase boundary (TPB) into the electrode bulk and (2) to reduce the mismatch in thermal expansion coefficients between the electrode and electrolyte materials, ensuring good mechanical compatibility.

It is well established that even the material morphology strongly affects the electrode performance. Focusing on nanofibers, recent studies demonstrate better electrochemical performance in comparison to granular materials and nanorods of similar size [22,23]. The cited nanofibers were produced by electrospinning after careful optimization of the experimental parameters [24]; the method comes in fact as one of the techniques of choice when dealing with the preparation of one-dimensional materials, such as nanotubes, nanowires, and nanorods [25–27], and also for the specific application of the electrospun nanofibers in SOFCs [28].

Electrochemical impedance spectroscopy (EIS) is commonly used to determine the polarization resistance R_p of IT-SOFCs electrodes by lumping together different sources of loss [29]. Results from this technique are interpreted by using equivalent circuit (EC) modeling, where different EC elements are used to describe the physico-chemical processes occurring both at the electrolyte/electrode interface and in the bulk of the electrode. MIEC cathodes, like LSCF, are generally described using a combination of the RQ element, representing the electrochemical process occurring through an interface, the Gerischer (G) element, representing the penetration of the electrochemical reaction into the electrode body thanks to simultaneous electronic and ionic charge transfer [30,31], and the Finite-Length-Warburg (FLW), representing diffusive effects in the electrode and the adjacent boundary layer. Interestingly, the EIS spectra obtained from LSCF nanofibers at different temperatures show a marked Gerischer-like behavior [31]. Instead, for powders, discordant results are reported in the literature, often showing a transition occurring at low temperature, usually around ~900 K [32]. The observed differences between powders and nanofibers allow to probe how morphology affect the electrode electrochemical performance. Indeed, the effects of the electrospinning synthesis route on the structure and properties of LSCF materials have not been explored in previous studies. Only one previous work derived crystalline properties from XRD experimental data of electrospun fibers with different compositions in the $La_{1-x}Sr_xCo_{1-y}Fe_yO_{3-\delta}$ system [33]. Nevertheless, the variation of these properties with temperature was not investigated, nor the possible correlation with the electrical conductivity of the fibers, which was also measured.

This work experimentally investigates, as a function of temperature, structural, microstructural and electrochemical impedance properties of LSCF electrodes, both in the form of electrospun nanofibers (in-house preparation) and granular powders (commercial), the latter serving as a control sample. Unlike previous research aiming to prove the superior electrochemical performance of LSCF nanofibers over powders [23,34], the present investigation focuses on unravelling possible correlations between morphology, crystal structure, and electrocatalytic features, with a particular focus on the role of the R → C transition, merging together results from synchrotron x-ray diffraction and EIS tests. This work is intended to be the first attempt to correlate crystal structure data and electrocatalytic results obtained from LSCF perovskites.

2. Materials and methods

2.1. LSCF nanofibers and powders

LSCF nanofibers with formula $La_{0.6}Sr_{0.4}Co_{0.2}Fe_{0.8}O_{3-\delta}$ were produced in-house. The synthesis started with the preparation of the metal precursors solution, needed to feed the electrospinning equipment. To this purpose, metal nitrates [$Sr(NO_3)_2$, $La(NO_3)_3$ $6H_2O$, $Fe(NO_3)_3$ $9H_2O$, $Co(NO_3)_2$ $6H_2O$, 99.9% wt., Sigma-Aldrich] were dissolved in deionized water. Polyvinylpyrrolidone (PVP, Mw = $1.3*10^6$ g/mol, Sigma-Aldrich), acting as a carrier polymer, was also added; its amount was 10% wt. of the whole solution weight. The solution was homogenized by ball-milling. The amounts of metal nitrates were chosen to reproduce the desired molar ratios, namely 6:4 and 2:8 for La:Sr and Co:Fe, respectively. Further details about the preparation of the LSCF starting solution are reported in [22,35].

Nanofibers were electrospun (RT Advance, Linari Engineering, Pisa, Italy) on a rotating cylinder with a solution flow rate of 0.3 mL/h, applied voltage of 4 kV/cm, and relative environment humidity (RH) set at 25%. The so-obtained tissues underwent a thermal treatment in air up to 1073 K to eliminate the carrier polymer. The temperature was slowly increased (heating rate: 0.5 K/min) to promote the controlled decomposition of PVP, occurring in the 573–773 K range, and to provide sufficient time for the diffusion of the released gasses from the nanofibers inside.

For the sake of comparison, the whole study was also performed on a commercial LSCF granular powder (Sigma-Aldrich 704,288, median particle diameter d50 = 0.9 μm ± 0.2 μm, surface area 6 m^2/g ± 2 m^2/g).

2.2. Scanning electron microscopy analysis

The nanofiber morphology was evaluated through scanning electron microscopy coupled to an energy dispersive system (SEM-EDS) by a Zeiss Ultra 55 microscope; images were acquired by secondary electrons on the electrospun tissue before and after the thermal treatment. A ~10 nm thick layer of gold was sputtered onto the surface of raw fibers to improve their conductivity; on the contrary, sintered nanofibers were observed without coating. The acceleration voltage was set at 10 kV and 15 kV for the former and the latter, respectively: uncoated nanofibers need a higher voltage to provide images with a good resolution. The average nanofibers diameter, before and after the thermal treatment, was evaluated by using Diameter J, which is a plugin of the ImageJ software, on the acquired SEM images [36].

2.3. High-temperature synchrotron x-ray diffraction

The structural characterization was carried out by synchrotron x-ray diffraction at room and high temperature both on the LSCF sintered nanofibers and powders. Patterns were collected at the XRD1 beamline of the Elettra Synchrotron facility located in Trieste (Italy). The heat-treated LSCF nanofibers and the commercial LSCF powders were separately crumbled and ground in an agate mortar, and subsequently put in quartz capillaries with an inner diameter of 0.5 mm. Patterns were collected for both samples at room temperature (RT), 773 K, 873 K, 973 K, 1073 K, and 1173 K in the 5–55° 2θ range, with the energy of the incident x-ray beam set at 18 keV (corresponding to $\lambda = 0.68881$ Å); samples were heated by a blower and maintained in rotation during measurements. LaB_6 was used as an external standard both to refine some geometrical parameters (sample to detector distance, detector orthogonality) and to calculate the instrumental resolution function, needed to separate the sample and the instrument contribution to peak broadening. The beamline is equipped with a Pilatus 2 M detector, having 1475 × 1679 squared pixels with a size of 0.172 mm; during acquisitions, samples were placed at 85 mm from the detector; the spot size was 0.15 × 0.15 mm. The undesired fluorescence effect caused by the presence of Sr and of the other elements was reduced by setting the Pilatus threshold at 16750 eV so that less energetic photons were discarded by the detector. Samples were analyzed near the tip of the capillary, where the best packing is expected, and the exposure time was 60 s for LSCF nanofibers and LaB_6, and 120 s for the LSCF powder sample. The so-acquired 2D data were converted to 1D using the fit2D software [37], setting 2500 as the binning parameter. The FullProf software [38] was employed to analyze diffraction patterns and perform refinements through the Rietveld method; the WinPlotR tool [39] was used to represent diffractograms.

2.4. Electrochemical impedance spectroscopy

The electrocatalytic properties of the LSCF nanofibers and powders as cathodes for IT-SOFCs were evaluated through EIS. Symmetrical electrochemical cells were prepared using $Ce_{0.9}Gd_{0.1}O_{1.95}$ (Gadolinium-doped ceria, GDC) circular disks of approximately 325 ± 25 μm thickness and 13 ± 2 mm diameter as electrolytes.

To fabricate the nanofibers-based symmetrical cells, pre-cut circles of LSCF nanofiber tissues were applied on both sides of the GDC electrolyte disks. To ensure a good adhesion, the side of the LSCF electrode to be applied on the GDC disk was slightly humidified with the sol-gel electrospinning feeding solution. In that way, the formation of an interface between electrode and electrolyte was promoted, and nanofibers maintained to a large extent their fibrous structure. Finally, prior to the electrochemical tests, the cells were fired *in situ*, *i.e.* inside the EIS equipment, at the maximum temperature of 1223 K for 3 h. The heat-treated electrodes had a diameter of 0.64 cm (electrode area 0.32 cm^2). The morphological characterization of these cells suggests that after application on the electrolyte, fibers maintain an in-plane orientation with the electrolyte disk itself [22].

To manufacture the powder-based electrodes, the LSCF powder was dispersed in α-terpinol and symmetrically deposited onto the GDC electrolyte. The so obtained cells were then fired within a furnace, following the same heating program adopted for the nanofiber-based ones. After the heat treatment, electrodes had a diameter of 0.79 cm (electrode area 0.49 cm^2). Afterwards, cells were mounted in a four-sample set-up where each cell was fixed between two gold meshes, also acting as current collectors. The set-up was placed into a furnace, sealed, and attached to the gas supply system.

EIS spectra were recorded from 1123 K down to 823 K in steps of 50 K, while samples were exposed to a continuous oxygen/argon flow, with $p_{O2} = 0.2$ atm and $p_{Ar} = 0.8$ atm. Spectra were recorded in the frequency range from 1×10^{-2} Hz to 1×10^{6} Hz with a 10 mV voltage amplitude using a Gamry Reference 600 potentiostat. Kramers-Kronig analysis was accomplished to check linearity, stability, and causality. For frequencies lower than 10^5 Hz, the error on the impedance experimental measurements was <1%, while for frequencies between 10^5 and 10^6 Hz the experimental error was <10% [31]. The high-frequency inductance of the experimental apparatus, evaluated separately through a blank test as 4.9×10^{-8}H, was subtracted from the raw experimental data.

3. Results

3.1. Morphology of nanofibers and powders

SEM microphotographs, taken by secondary electrons on as-spun (a-b) and annealed (c-d) LSCF nanofibers, are reported in Fig. 1 at different magnifications. Raw LSCF nanofibers are continuous and well elongated, and these properties persist after thermal treatment.

The average diameter of LSCF nanofibers before and after the thermal treatment was investigated as well, using the software ImageJ. The outcome of the analysis appears in Fig. 2, where the relative frequency of specific diameter ranges is reported. Image analyses were carried out on Fig. 1a for the as-spun and *1c* for the heat-treated nanofibers, as well as on additional SEM images acquired on the same samples with the same magnification. The highest frequency for as-spun LSCF nanofibers occurs at around 0.41 μm, while for the heat-treated ones it falls at ~0.19 μm, thus suggesting a 50% reduction of the average fiber diameter as a consequence of the elimination of PVP promoted by the thermal process [21].

SEM microphotographs taken by secondary electrons on LSCF commercial powders are reported in Fig. 3 with different magnifications.

3.2. Structure and microstructure of nanofibers and powders

The results of the present investigation substantially confirm the literature data on the crystal structure adopted by the LSCF perovskite phase, reported stable at room temperature in the rhombohedral form; this structure is maintained up to high temperature. Diffraction patterns collected at different temperatures on (a) nanofibers and (b) powders are shown in Fig. 4, with highlighted the Miller indices associated to the rhombohedral $R\bar{3}c$ space group. For nanofibers, some low-intensity peaks attributable to tiny amounts of Al_2O_3 (contaminant from alumina crucible used during sintering), are visible. This extra phase is stable and non electrochemically active.

The rhombohedral structure typical of LSCF at room temperature can be considered as formally deriving from the ideal cubic perovskite through a distortion due to the partial substitution of La^{3+} by the larger Sr^{2+} cation in the A position; moreover, the partial replacement of a trivalent cation by a lower-valence one brings about the occurrence of oxygen vacancies and induces mixed ionic and electronic conductivity. A representation of the cubic and rhombohedral structures of LSCF is shown in Fig. 5; the corresponding crystal data are collected in Table 1.

As can be seen, both structures are based on the three-dimensional interconnection of oxygen octahedra, centered by the Fe/Co atoms occupying the B site. Octahedra are linked together by sharing their vertices, so that each octahedron is connected to 6 others; the resulting 3D framework leaves the dodecahedral cavities where the largest A atoms can settle. The similarity between the two structures becomes much more evident if the cubic and the rhombohedral cells are viewed along the [111] and the [001] directions, respectively (see Fig. 6): in this layout the octahedra show one of the triangular faces and the connection with the 6 neighboring octahedra is clearly visible. While in the cubic structure all the octahedra are perfectly regular and isooriented, in the rhombohedral deformation one half of the octahedra are rotated by nearly 20° with respect to the second half.

To quantify the degree of deformation of the rhombohedral structure with respect to the ideal cubic one, a deviation parameter, as defined by the following expression [42], can be estimated:

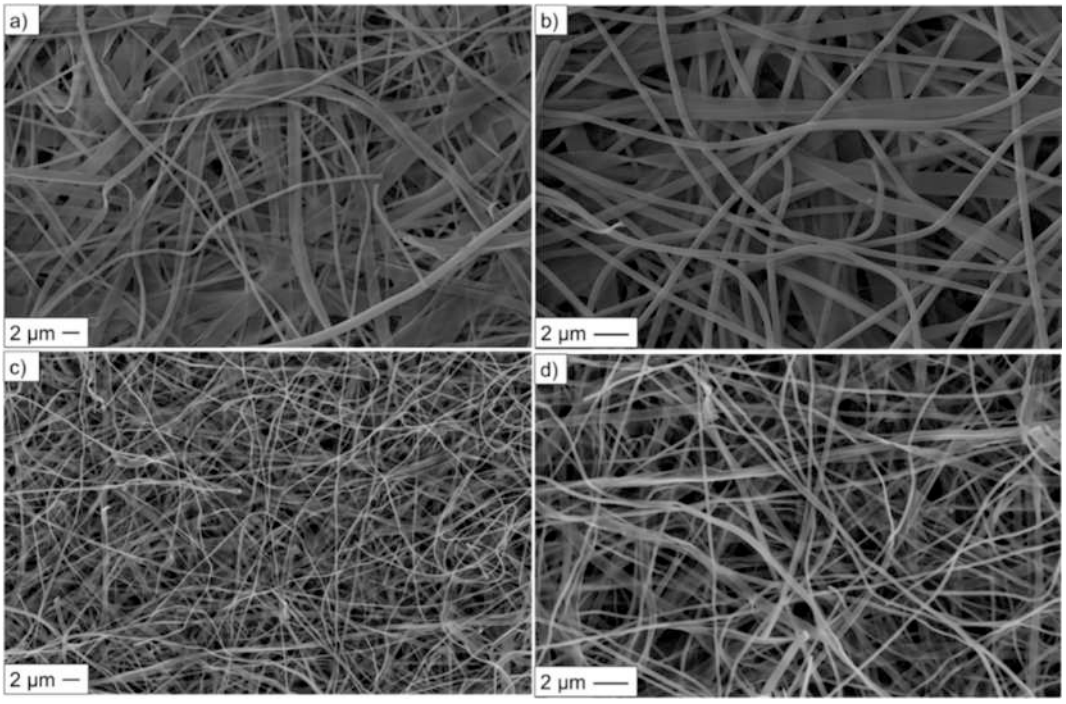

Fig. 1. SEM microphotographs of LSCF nanofibers taken by secondary electrons before (a-b) and after (c-d) thermal treatment.

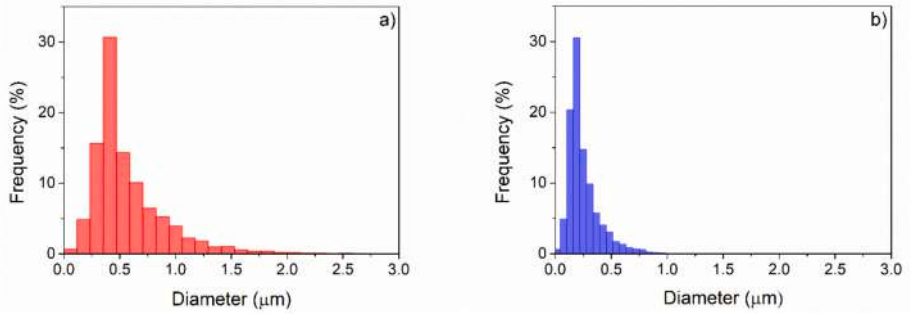

Fig. 2. Average diameter of nanofibers as resulting from the image analysis of samples before (a) and after (b) thermal treatment.

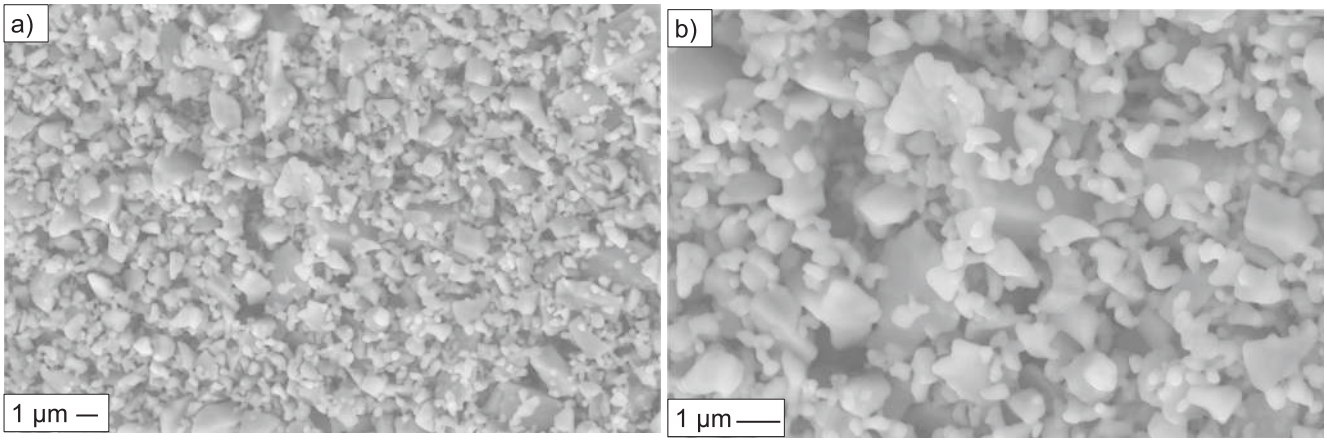

Fig. 3. SEM microphotographs of LSCF powders taken by secondary electrons.

$$\Delta x = \frac{\Sigma\left[m\sqrt{(x_1 - x_2)^2 + (y_1 - y_2)^2 + (z_1 - z_2)^2}\right]}{\Sigma m} \quad (1)$$

Here, the differences in the coordinates of all atoms are taken into account: x_1, y_1, z_1 are the coordinates of an atom in the first structure, and x_2, y_2, z_2 are those of the corresponding atom in the second

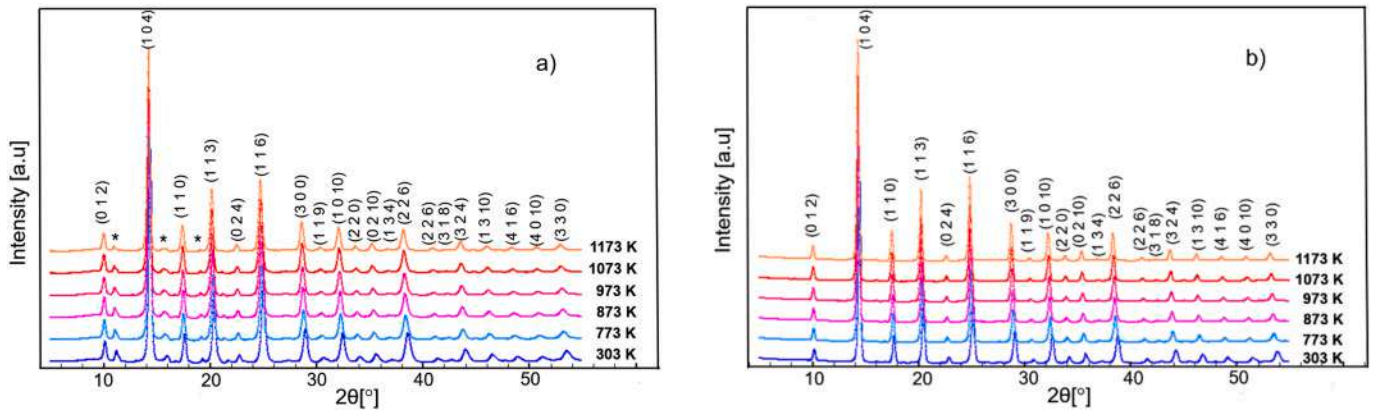

Fig. 4. Stacked diffraction patterns of LSCF (a) nanofibers and (b) powders at room and high temperature.

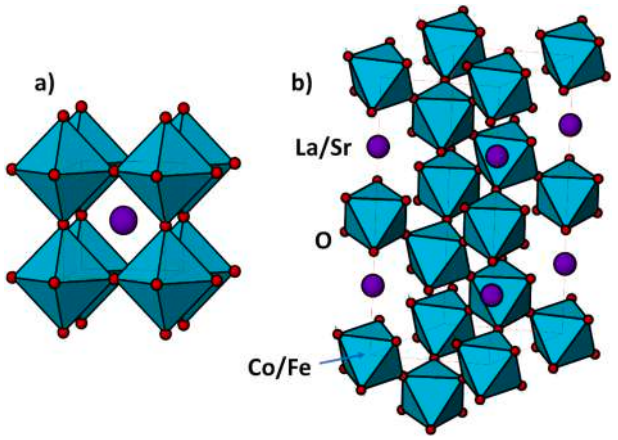

Fig. 5. Representation of the (a) cubic and (b) rhombohedral structure of LSCF. Large and small spheres correspond to La/Sr and O atoms, respectively; the octahedral environment of Co/Fe is highlighted. Drawings were produced with ATOMS, by Shape Software.

structure; *m* is the multiplicity of the Wyckoff position and the sum is referred to all atoms in the asymmetric unit. To be properly compared, the two structures must be standardized in the same way, so in the specific case both structures are transformed into the corresponding primitive rhombohedral cell. The 3 × 3 matrices allowing this reticular transformation are reported in Table 2, together with the list of coordinates after transformation and the relative deviation parameter: this value is very small, indicating that the two structures are strongly similar. It is also noteworthy the close similarity in the cell parameters of the primitive rhombohedral cells, and the exact value of 60° assumed by the α angle when the cubic symmetry governs. For this reason, the deviation from 60° of the α angle can be taken as an index of the rhombohedral character of the structure, and ultimately the variation with temperature of the α angle may be analyzed to identify the R → C structural transition.

All diffraction data were analyzed through the Rietveld method [43]: the basic model used for the refinements was the rhombohedral one, in agreement with the literature data reported in Table 1. However, since the exact temperature of the R → C transition is not known, for both samples at higher temperatures, the cubic as well as the rhombohedral models were considered. The obtained results confirmed the substantial correctness of the rhombohedral structure for the nanofiber sample at all temperatures and for the powder sample up to $T = 973$ K; at the two highest temperatures (1073 and 1173 K) the rhombohedral structural model could not be forced to converge during refinements, while the cubic one proved to be the most adequate to describe the atomic arrangement. Besides the structural parameters (lattice parameters, *x* fractional atomic coordinate and occupancy factor of oxygen atoms, the isotropic atomic displacement parameters B_{at}), the scale factor and the peak profile parameters (Caglioti U, V and W, η [the Pseudo Voigt mixing parameter], Y [the θ dependence of η], and two asymmetry parameters) were refined. The background was optimized by linear interpolation of a set of ~50 points taken from the experimental pattern.

The Rietveld plot of LSCF powders analyzed at room temperature is reported in Fig. 7 as a representative example. The final refined structural parameters, namely cell parameters, the *x* fractional coordinate of oxygen, and the atomic displacement parameter B_{at}, together with the values of the R_B agreement factor, are collected for both samples in Table 3; the refined oxygen occupancies are not reported here, but shown in Fig. 10a.

In Fig. 8 the trend of cell volumes of both nanofibers and powders is reported as a function of temperature. A linear increase is observed for both morphologies, but fibers are characterized by a cell volume significantly higher than powders.

Room and high temperature structural data allow to calculate the coefficient of thermal expansion (CTE). The linear CTE is an intrinsic property of materials that provides information regarding the extent of expansion upon heating at a given temperature. CTE of a solid material can be defined as:

$$CTE = \frac{1}{a_0}\,\frac{a_T - a_0}{T - T_0} \qquad (2)$$

Table 1
Structural information of the two crystal structures typical of LSCF.

Crystal System	Space group	Pearson's code prototype	Atom	Wyckoff position	Fractional coordinates	Cell parameters [Å]		Ref
						a	*c*	
Rhombohedral	$R\bar{3}c$	*hR*30-$LaAlO_3$	La/Sr	6*a*	0, 0, 1/4	5.5355	13.5484	[40]
			Fe/Co	6*b*	0, 0, 0			
			O	18*e*	~0.46, 0, 1/4			
Cubic	$Pm\bar{3}m$	*cP*5-$CaTiO_3$	La/Sr	1*b*	1/2, 1/2, 1/2	3.878		[41]
			Fe/Co	1*a*	0, 0, 0			
			O	3*d*	1/2, 0, 0			

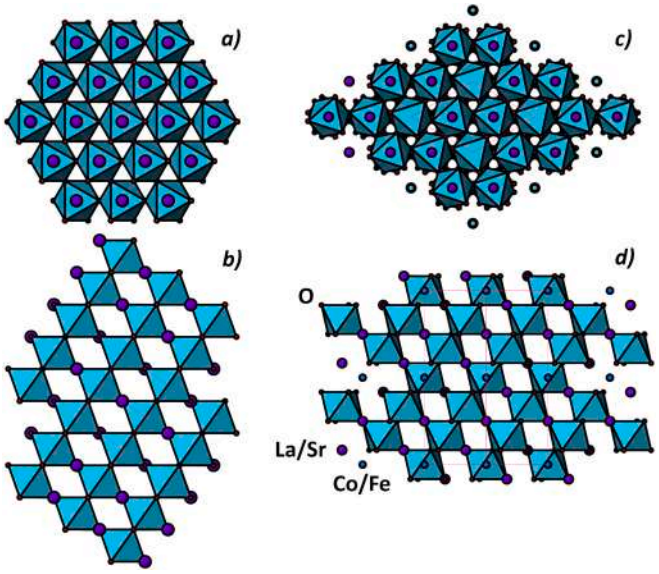

Fig. 6. Comparison between cubic and rhombohedral structures of LSCF, viewed along the crystallographic direction that better highlights the similarity of the two structural arrangements: a) and b) correspond respectively to the projection of the cubic structure along the [111] crystallographic direction and along its perpendicular orientation, the [−101] direction; c) and d) are the projections along the [001] and the [110] directions in the rhombohedral structure. The octahedra around Co/Fe are highlighted; La/Sr and O atoms are represented in blue and red, respectively. Drawings were produced with ATOMS, by Shape Software. (For interpretation of the references to colour in this figure legend, the reader is referred to the web version of this article.)

where T_0 is room temperature, T is the analysis temperature (1173 K in this work), a_0 and a_T are the cell parameter at room temperature and at T, respectively. Cell parameters were obtained from Rietveld refinements as the cubic root of the refined cell volume for both the R and the C structure. The CTE values calculated for nanofibers and powders are respectively $13.2*10^{-6}$ and $14.2*10^{-6}$ K^{-1}. LSCF fibers have thus less tendency than powders to expand with increasing temperature. The value of CTE is of crucial importance in relation to the other components of the cell, such as for instance the electrolyte, since minimizing the CTE discrepancy between adjacent layers entails a significant increase of mechanical stability, and hence of device durability [44,45]. In this respect, it is worth mentioning that the CTE value of GDC, the typical ceramic electrolyte used in solid oxide fuel cells, ranges between $12*10^{-6}$ and $10*10^{-6}$ K^{-1}, depending on the Gd content [46]; therefore, LSCF nanofibers appear as the most proper morphology to be used in GDC-based cells.

The values of the α angle derived after the Rietveld refinements, following the transformation matrices listed in Table 2, are reported in Fig. 9 as a function of temperature for both nanofibers and powders. The plot deserves some comments. First of all, it can be observed that powders exhibit a progressive decrease of the angle toward the value typical of the cubic structure (60°), which is reached at temperatures close to 1000 K. This result is in very good agreement with literature data [47], also reported in the diagram as a term of comparison. Nevertheless, the actual element of novelty regards the behavior of the nanofiber sample: in this case a progressive gentle decrease of the α angle with increasing temperature is observed, but the value of the cubic structure is by far not reached, even at the highest temperature considered, which leads to conclude that the R → C transition does not occur within the entire studied temperature range. Although the reasons for the behavior of LSCF nanofibers are not known, it is clear that they must be rooted in the electrospinning process.

Oxygen occupancies, obtained as a result of Rietveld refinement for both morphologies, are reported in Fig. 10a as a function of temperature. A progressive decrease of the cited parameter with increasing temperature can be observed for both nanofibers and powders; nevertheless, while fibers exhibit a regular decrease up to the highest temperature, in powders a sudden drop of the oxygen occupancy value occurs at ~1000 K, namely in correspondence of the previously discussed R → C transition. Below this temperature nanofibers present oxygen occupancies significantly smaller than powders; this evidence can be considered the reason why the crystal cell of fibers results larger than the powders one (see Fig. 8): the presence of vacancies within the lattice strongly reduces the electrostatic attraction between cations and anions, and enhances the electrostatic repulsion between cations, thus inducing an enlargement of the cell. Interestingly, the described trend is in nice agreement

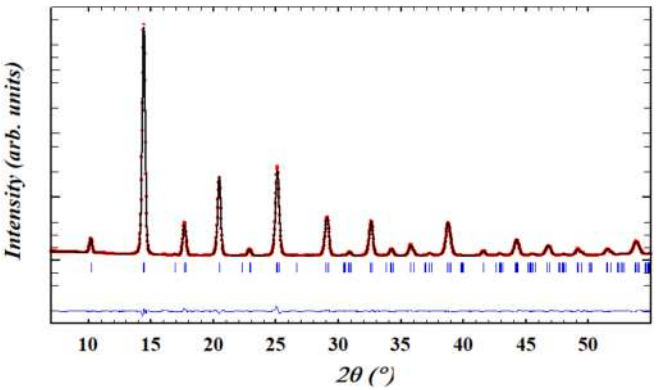

Fig. 7. Rietveld plot of powders at room temperature. The dotted (red) and the continuous (black) lines are the experimental and the calculated diffractogram, respectively; the lower line is the difference curve; vertical bars indicate the calculated positions of Bragg peaks of the rhombohedral cell. (For interpretation of the references to colour in this figure legend, the reader is referred to the web version of this article.)

Table 2
Crystal data of cubic and rhombohedral structures [40,41] described according to conventional cells and to the rhombohedral primitive (R_p) cells. Matrices correspond to the conventional→R_p cell transformation. Δx is the deviation parameter, defined by Eq. (1).

Conventional cell	Atomic coordinates	Rhombohedral primitive cell	Transformation matrix	Transformed coordinates	Δx
$Pm\bar{3}m$ $a = 3.878$ Å	La/Sr 1*a* $(\frac{1}{2},\frac{1}{2},\frac{1}{2})$ Co/Fe 1*b* (0,0,0) O 3*d* $(\frac{1}{2},0,0)$	$R\bar{3}c$ $a = 5.4843$ Å $\alpha = 60°$	$\begin{pmatrix}1 & 0 & 1\\1 & 1 & 0\\0 & 1 & 1\end{pmatrix}$	La/Sr 2*a* $(\frac{1}{4},\frac{1}{4},\frac{1}{4})$ Co/Fe 2*b* (0, 0, 0) O 6*e* $(\frac{1}{4},\frac{3}{4},\frac{1}{4})$	
$R\bar{3}c$ $a = 5.5355$ Å $c = 13.5484$ Å	La/Sr 6*a* $(0,0,\frac{1}{4})$ Co/Fe 6*b* (0, 0, 0) O 18*e* $(0.46,0,\frac{1}{4})$	$R\bar{3}c$ $a = 5.5326$ Å $\alpha = 60.04°$	$\begin{pmatrix}\frac{2}{3} & -\frac{1}{3} & -\frac{1}{3}\\\frac{1}{3} & \frac{1}{3} & -\frac{2}{3}\\\frac{1}{3} & \frac{1}{3} & \frac{1}{3}\end{pmatrix}$	La/Sr 2*a* $(\frac{1}{4},\frac{1}{4},\frac{1}{4})$ Co/Fe 2*b* (0, 0, 0) O 6*e* $(0.21,\frac{3}{4},0.29)$	0.034

Table 3
Refined structural parameters of LSCF nanofibers (N) and LSCF powders (P) at different temperatures.

Morphology	T [K]	Cell parameters [Å]		x_O	B_{at} [Å^2]			R_B[1]
		a	c		La/Sr	Fe/Co	O	
N	303	5.5236(6)	13.426(3)	0.454(2)	0.09(5)	0.25(5)	0.5(2)	2.43
P		5.4984(2)	13.3745(8)	0.4574(7)	0.53(2)	0.39(2)	0.49(7)	1.23
N	773	5.5536(5)	13.512(3)	0.453(1)	0.65(5)	0.80(4)	1.0(2)	2.24
P		5.521(2)	13.516(8)	0.4649(9)	1.24(2)	0.83(2)	1.46(7)	0.938
N	873	5.5612(5)	13.535(3)	0.456(2)	0.78(5)	0.93(4)	1.2(2)	2.32
P		5.527(2)	13.550(8)	0.468(8)	1.41(2)	0.94(2)	1.74(9)	1.04
N	973	5.5682(6)	13.559(3)	0.456(2)	0.93(5)	1.04(4)	1.4(2)	2.24
P		5.540(3)	13.551(9)	0.470(1)	1.59(2)	1.05(2)	1.94(9)	2.04
N	1073	5.5747(6)	13.584(3)	0.456(2)	1.13(4)	1.17(4)	1.5(1)	2.03
P		3.92107(5)	–	–	1.80(2)	1.19(2)	2.08(6)	1.99
N	1173	5.5813(5)	13.608(3)	0.455(1)	1.37(3)	1.32(3)	1.5(1)	1.73
P		3.92685(5)	–	–	2.01(2)	1.33(2)	2.24(6)	2.07

[1] Values are calculated as $R_B = \frac{\sum_k |I_{k,obs} - I_{k,calc}|}{\sum_k |I_{k,obs.}|}$.

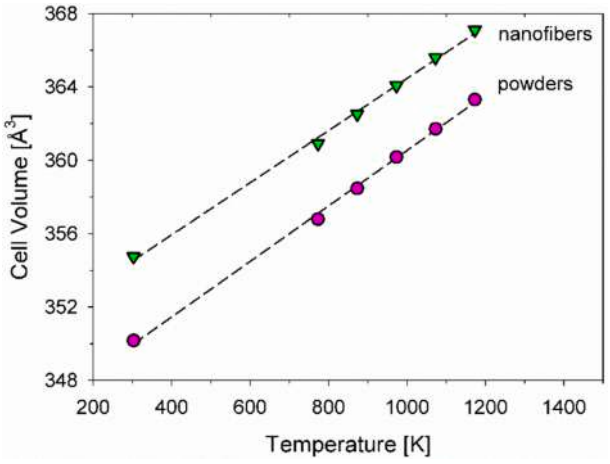

Fig. 8. Refined cell volumes of LSCF nanofibers and powders. Dashed lines are regression lines interpolating experimental data. Error bars are hidden by data markers. Values at 1073 and 1173 K were obtained multiplying by 6 the cubic cell volume, to make data comparable to the ones of rhombohedral samples.

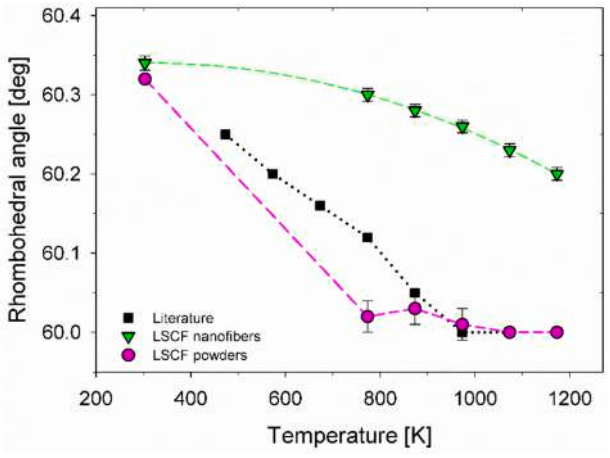

Fig. 9. Trend of the α angle in powders and nanofibers as a function of temperature. Data of powders at 1073 and 1173 K are fixed at 60° and therefore devoid of error bars. Data taken from the literature [47] are reported too for the sake of comparison.

with the results of TGA measurements performed by Tai et al. [12]. The significantly lower oxygen occupancy values of fibers with respect to powders up to ~1000 K suggest a higher concentration of oxygen vacancies in the former and allow to presume a higher conductivity. Furthermore, since oxygen vacancies are reactants in the electrochemical reactions [48], lower oxygen occupancy is expected to enhance the electrochemical reactions and, more generally, the electrochemical performance.

As a direct consequence of the oxygen occupancy reduction, the average atomic volume of both fibers and powders increases with rising temperature and presents a sudden increase in powders at the R → C transition. This parameter, intended as the cell volume divided by the number of atoms populating the cell, was calculated taking into account the refined oxygen content, and it is reported in Fig. 10b.

Table 3 also reports the refined values of the atomic displacement parameter B for each involved atom. In agreement with the atomic mass of the elements, the B value of oxygen, namely of the lightest atom, is the highest one; moreover, as expected, all values increase with increasing temperature. It is also noteworthy that the displacement parameter of all atoms is higher in powders than in fibers.

To obtain information on the microstructure of LSCF, the sample-dependent broadening (β) of the XRD peaks was firstly separated by the instrument-dependent contribution, and then analyzed according to the Williamson-Hall (W—H) approach [49,50]. Following this method, the quantity $\frac{\beta cos\theta}{\lambda}$ can be obtained from the equation below (further details about the relevant equations are reported in ref. [51]):

$$\frac{\beta cos\theta}{\lambda} = \frac{0.9}{D} + 2\varepsilon d^* \quad (3)$$

where d^* is the interplanar distance in the reciprocal space for each considered family of crystallographic planes, D represents the average domain size and ε is the upper limit of microstrain. The plot of $\frac{\beta cos\theta}{\lambda}$ *vs.* d^* results in a straight line in the case of isotropic broadening, namely when the microstrain is independent of the crystal lattice direction. Slope and intercept give therefore an evaluation of the upper microstrain limit (ε) and average domain size (D), respectively. In Fig. 11 the W—H diagram of both nanofibers (a) and powders (b) is reported for each temperature: the linear trend obtained for every family of crystallographic planes points at a uniform anisotropic stress. It can be observed that regression lines fitting the refined $\frac{\beta cos\theta}{\lambda}$ values intercept the *y* axis at 0, meaning that no significant peak broadening can be attributed to the diffraction domain size.

The analysis of Fig. 11 reveals that for both morphologies the slope of regression lines, which is directly correlated to the microstrain arising within the structure, decreases with increasing temperature, as expected

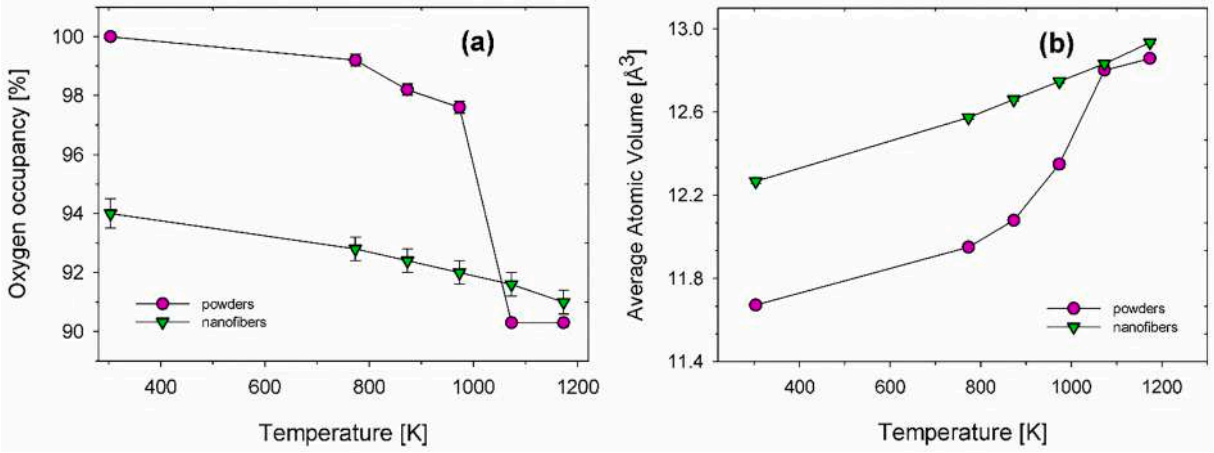

Fig. 10. (a) Percentage oxygen occupancy and (b) average atomic volume as a function of temperature for LSCF fibers and powders. Error bars are hidden by data markers; lines connecting experimental data are a guide for the eye.

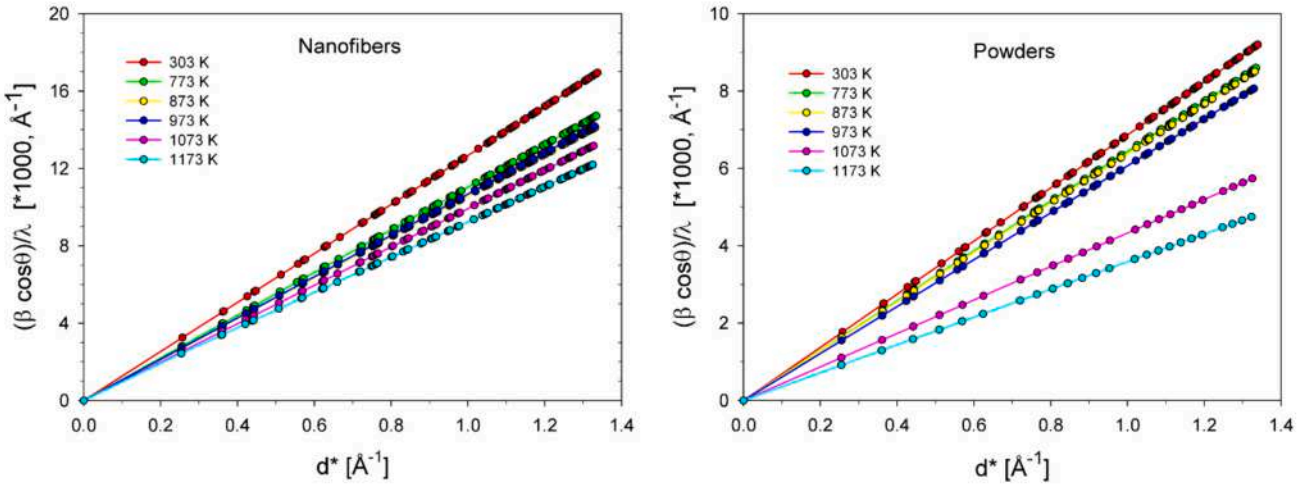

Fig. 11. Williamson-Hall plots at different temperatures for LSCF nanofibers (left) and LSCF powders (right).

from the effect of stress release due to the cell enlargement. Nevertheless, while in nanofibers a regular decrease is observed, in powders regression lines give rise to a strong slope reduction occurring at ~1073 K, namely at the temperature marking the R → C transition. In this respect, the R → C transition can be deemed as a way to release the internal tension of the structure through the sudden decrease in microstrain taking place at the transition temperature. This issue is observable in Fig. 12, where the ε ‰ microstrain is reported as a function of temperature for both morphologies. Fig. 12 also highlights the higher values of microstrain in nanofibers than in powders. Bearing in mind that microstrain is a local deviation of d-spacings from the mean value caused by local defects, this evidence can be correlated with the higher number of vacancies occurring in nanofibers, as testified by the trend of oxygen occupancy *vs.* temperature appearing in Fig. 10a.

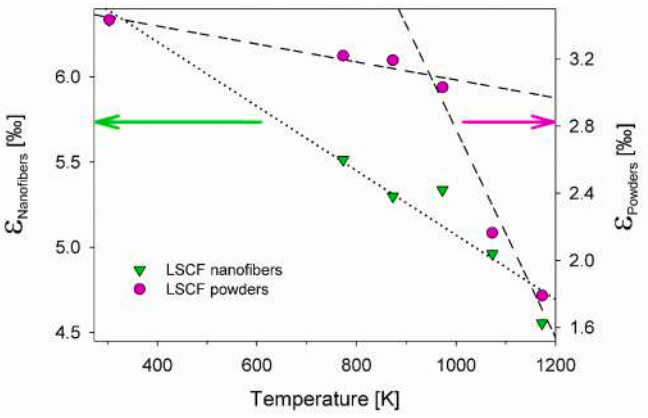

Fig. 12. Plot of the upper limit of isotropic strain ε [‰] *vs.* temperature in powder and nanofiber samples. Two different scales are used for the *y*-axis to ensure an easier comparison between the two morphologies. Data at 303 K appear superimposed due to the different scales.

3.3. ORR electrocatalytic activity of nanofibers and granular powders

The electrochemical properties of LSCF nanofibers and granular powders when used as cathodes in IT-SOFCs have been investigated in several works [23,32,34]. EIS has often been used to experimentally evaluate the overall electrode polarization resistance R_p and to obtain information about the processes occurring within the electrodes. Equivalent circuit modeling (ECM) is a useful instrument in this respect, since it enables to build a model where each process is associated to an

equivalent circuit element. The ECM methodology has been developed to study a variety of processes occurring in electrochemical systems [29]. It is based on the idea of schematizing the electrochemical cell as an electrical circuit. In MIEC materials, such as LSCF, simultaneously presenting ionic and electronic conductivities, the electrochemical reaction is expected to develop at the electrode/electrolyte interface, and also in the interior of the electrode, *i.e.* in the electrode bulk. In terms of ECM, it has been demonstrated that the overall electrode can be modeled as one (or more) RQ elements in series with a Gerischer (G) element [31]. The analytical equation of the inductance (Z) of the RQ element is:

$$Z(\omega) = \frac{1}{R^{-1} + Q(j\omega)^{\alpha}} \tag{4}$$

where ω is the radial frequency, R is the resistance associated with the charge transfer process, Q is the capacitance of the electrochemical double layer established at the interface through which the electrochemical reaction takes place, and α is a phenomenological parameter. The equivalent or apparent capacitance is defined as follows:

$$Q_{equiv} = \frac{(QR)^{1/\alpha}}{R} \tag{5}$$

The analytical equation of the inductance of the G element is:

$$Z(\omega) = \frac{1}{Y\sqrt{(k + j\omega)}} \tag{6}$$

where k is related to oxygen surface exchange coefficient and Y embeds structural parameters and solid-phase oxygen diffusion coefficients. The Gerischer impedance element was originally proposed for a mercury electrode in a liquid electrolyte, where it was demonstrated to provide a suitable representation of the phenomenon of distributed electrochemical reaction coupled to simultaneous mass diffusion [52]. Nevertheless, it is currently widely applied to MIECs, where it accounts for distributed electrochemical reaction coupled to simultaneous charge transfer [21,22,53]. In previous works, it was shown that the Gerischer element can be applied to nanofiber LSCF electrodes [22,31].

EIS experimental data were fitted by the EC model equations using a mathematical routine that adjusts model parameters to achieve error minimization. The complex non-linear least squares (NLLS) fitting method [54], implementing the Levenberg-Marquardt (LM) algorithm is often adopted [55]. The software Elchemea [56] was used to implement the EC model adopted in the present work, and to fit it to the EIS experimental data. All impedance values reported in the paper are area specific, expressed in [Ω cm^2], obtained by multiplying the experimentally measured value by the electrode area. The result is then divided by 2, since, in case of symmetrical cells, two identical electrodes are measured altogether.

Finally, with reference to the Nyquist representation of the EIS impedance data, the overall polarization resistance R_p of the electrode was evaluated as the difference between the low- and high-frequency intercepts with the real axis. Analogously, each single EC element used to fit EIS impedance data has an associated R_p, which in turn is the difference between its intercepts with the real axis.

In this work, the electrochemical properties of LSCF nanofiber- and powder-based cathodes were investigated using the EIS experimental technique coupled with ECM. The EC model proposed and utilized in this work is a simple series of five circuit elements:

$$Rs - RQ1 - RQ2 - G - FLW \tag{7}$$

where the circuit elements are listed in descending order of frequency.

The physical meaning of the different circuit elements is proposed below, and further justification is given *a posteriori* based on the EIS results. The physical meaning is explained with reference to Fig. 13, that contains schematizations of the electrode and the electrode/electrolyte interface. Fig. 13 is inspired by SEM pictures of the electrode/electrolyte interface reported in the literature for the LSCF nanofiber electrodes [22,34] and for the LSCF granular powder ones [32]. The physical meaning proposed for the different circuit elements is as follows:

- Rs is associated with the oxygen ion transfer through the GDC electrolyte;
- RQ1 is associated with the charge transfer from the electrolyte into the adjacent electrode layer. In more detail, this charge transfer occurs at the interface (surface path) between the electrolyte and the adjacent nanofibers or granules;
- G is associated with the simultaneous charge transfer and electrochemical reaction inside the electrode nanofibers or granules. This is a bulk path, namely a phenomenon occurring in the interior of fibers or granules, *i.e.* in the bulk of the LSCF material;
- RQ2 is associated with the charge transfer from one nanofiber to another, or from one granule to another, inside the electrode. This is a surface path since it occurs at the interface between one and another nanofiber/granule;
- The FLW element (not visualized in Fig. 13) is related to gas phase diffusion limitations. It has been demonstrated that the main limitations occur in the limiting gas diffusion layer adjacent to the electrode surface rather than in the electrode pores [30].

Fig. 14 reports the EIS experimental results obtained from LSCF nanofiber cathodes, together with EC fittings. These are typical EIS spectra obtained from LSCF cathodes [30,34,53]. More details are reported in previous works [22,31], whereas here the attention is restricted to the aspects exhibiting parallelism with the crystal structure properties discussed in the previous sections. EIS data for frequencies above $5*10^5$ Hz are not reported, since the impedance was very small and affected by a scattering attributed to the experimental error. No specific processes appear in the high-frequency range (frequency $f > 10^4$ Hz). This is in agreement with previous results obtained with LSCF nanofiber cathodes [22,31,34]. Thus, in Fig. 14, the Nyquist plot of the EIS experimental data at 823 K consists of a single arc, which in the left-hand region shows a straight line with a 45° slope with the real axis, which is the typical fingerprint of the Gerischer behavior [53]. Fig. 14 also shows that, with increasing temperature, this single arc progressively shrinks and distorts. By increasing temperature above 1023 K, the high-frequency straight line tends to bend, so that, at 1223 K, the arc is a

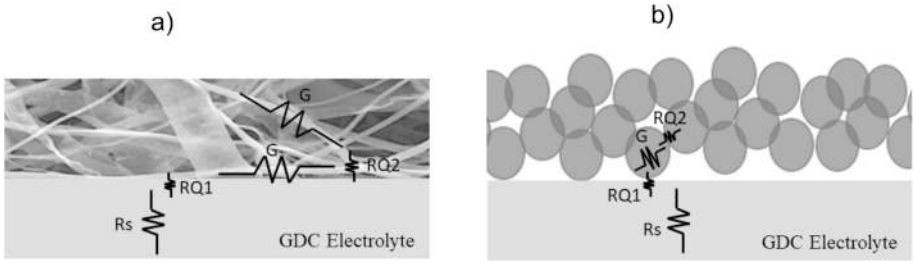

Fig. 13. Illustration of the physical meaning of the proposed Rs-RQ1-RQ2-G EC for (a) LSCF nanofiber and (b) LSCF granular powder electrodes.

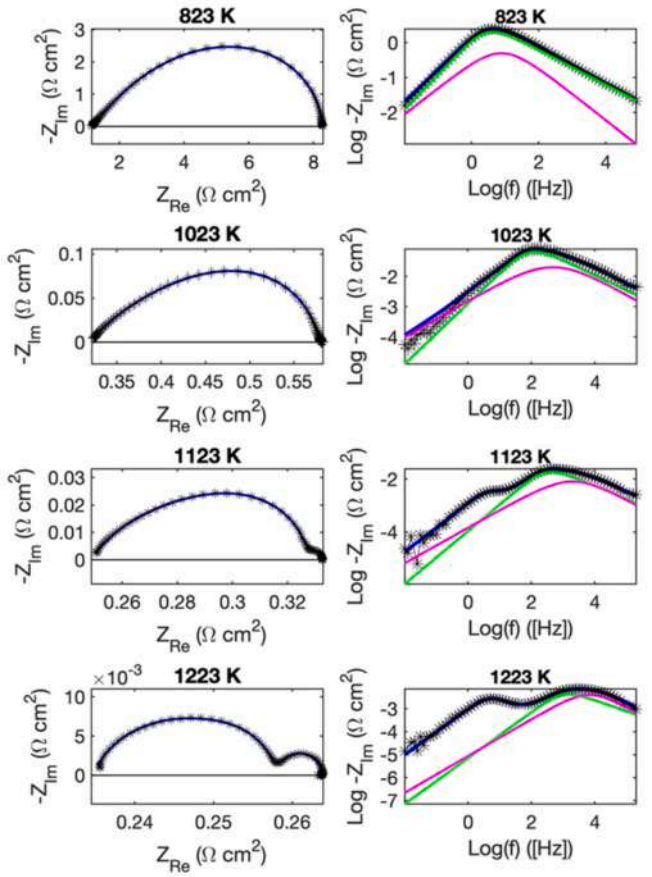

Fig. 14. EIS results obtained from LSCF nanofiber cathodes. Symbols: experimental data; blue line: fittings through the Rs-RQ2-G(-FLW) equivalent circuit. Left: Nyquist plots. Right: Bode plots, also displaying the individual contributions of the RQ2 (magenta line) and G (green line) circuit elements. (For interpretation of the references to colour in this figure legend, the reader is referred to the web version of this article.)

hybrid between Gerischer and RQ, resulting in a depressed semicircle, identified in the past as 'depressed Gerischer' [31]. In addition, by increasing temperature above 1023 K, the shrinkage of the high-frequency arc reveals a second, low-frequency arc. The size and shape of this low-frequency arc do not change significantly with temperature, which suggests that this arc is related to the physical process of gas phase diffusion [30]. Correspondingly, in Bode plots experimental data display at low temperature (823 K) a single process with a well-defined sharp maximum, clearly identifying one single time constant. By increasing temperature, the maximum decreases, and simultaneously it shifts toward higher frequencies, indicating that the process is thermally activated. A further remark about the high-frequency maximum is that, at high temperatures (from 1073 to 1223 K), this maximum is no longer sharp, but rather broad, and at the same time a curvature appears in the high-frequency part of the spectrum, which suggests that at least two processes overlap in the same frequency range. Still referring to Bode plots, at temperatures of 1023–1073 K and above, a second maximum becomes gradually visible in the low-frequency region, corresponding to the diffusive low-frequency arc already recognized in the Nyquist plots.

In Fig. 14, the fittings through the EC model are reported as well. The first remark is that the impedance of the RQ1 element obtained from the fittings was so small that it did not make sense to keep this component in the EC. The reason is that the RQ1 element is commonly used to fit a possible additional high-frequency arc, which is not present. This means that the physical phenomena associated with the RQ1 element are ideal, *i.e.* they generate a negligible impedance and energy loss. Therefore, it was possible to fit all the experimental EIS data with a simplified circuit, excluding the RQ1 element:

$$Rs - RQ2 - G - FLW \tag{8}$$

In Fig. 14, Bode plots display the individual contributions of the G and RQ2 components, and it is well visible that, at low temperature, the G element accounts almost completely for the impedance of the sample, the RQ2 contribution being practically negligible. By increasing temperature, the relative importance of the G contribution tends to decrease and, at 1223 K, the G and RQ2 contributions are comparable, with the maxima separated by one order of magnitude in frequency. Due to this, as already remarked, the G and RQ2 contributions merge, with one single maximum, rather broad in shape.

Figs. 15 and 16 report the EIS results obtained from LSCF granular powder electrodes in the 823–973 K and 1023–1223 K temperature ranges, respectively. These are typical EIS spectra obtained from LSCF cathodes [32,57]. In the high-frequency region a process is visible in the range between 10^4 Hz and 10^6 Hz, with summit frequency $f_{max} \sim 10^5$ Hz, which was not detected in the nanofiber LSCF electrode. The EIS data of the LSCF granular powders, on the contrary, display this clear additional arc in the Nyquist plot, which is well fitted by the RQ1 element of the EC. The literature regarding LSCF powder electrodes shows that in some cases this high-frequency arc is missing [32], whereas in other cases it is present [57], addressing it to the a charge transfer process through the electrode/electrolyte interface [58]. The values of equivalent (or apparent) capacitance of RQ1 are in the range 7×10^{-4} to 8×10^{-6} F

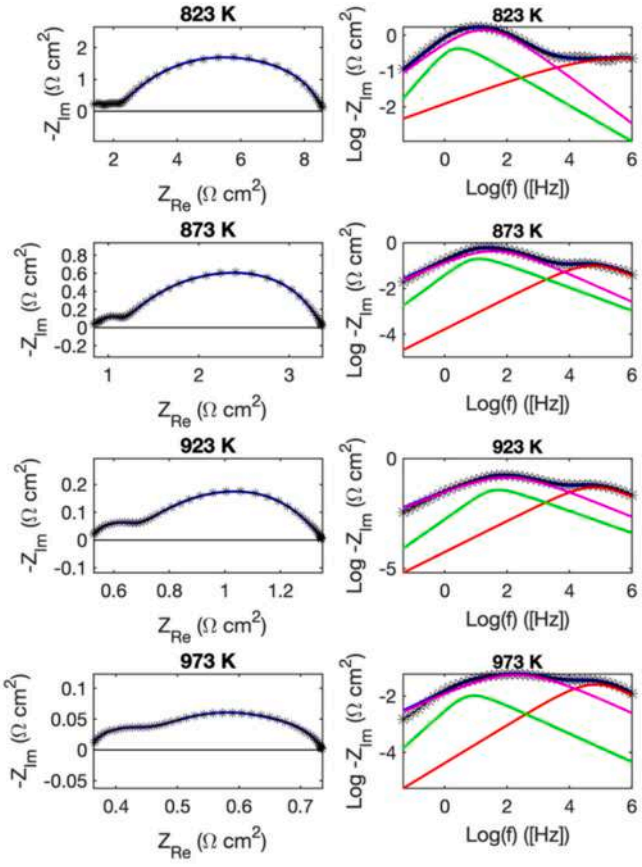

Fig. 15. EIS results obtained from LSCF granular powder cathodes between 823 K and 973 K. Symbols: experimental data; blue line: fittings through the Rs-RQ1-RQ2-G equivalent circuit. Left: Nyquist plots. Right: Bode plots, also displaying the individual contributions of the RQ1 (red line), RQ2 (magenta line), and G (green line) circuit elements. (For interpretation of the references to colour in this figure legend, the reader is referred to the web version of this article.)

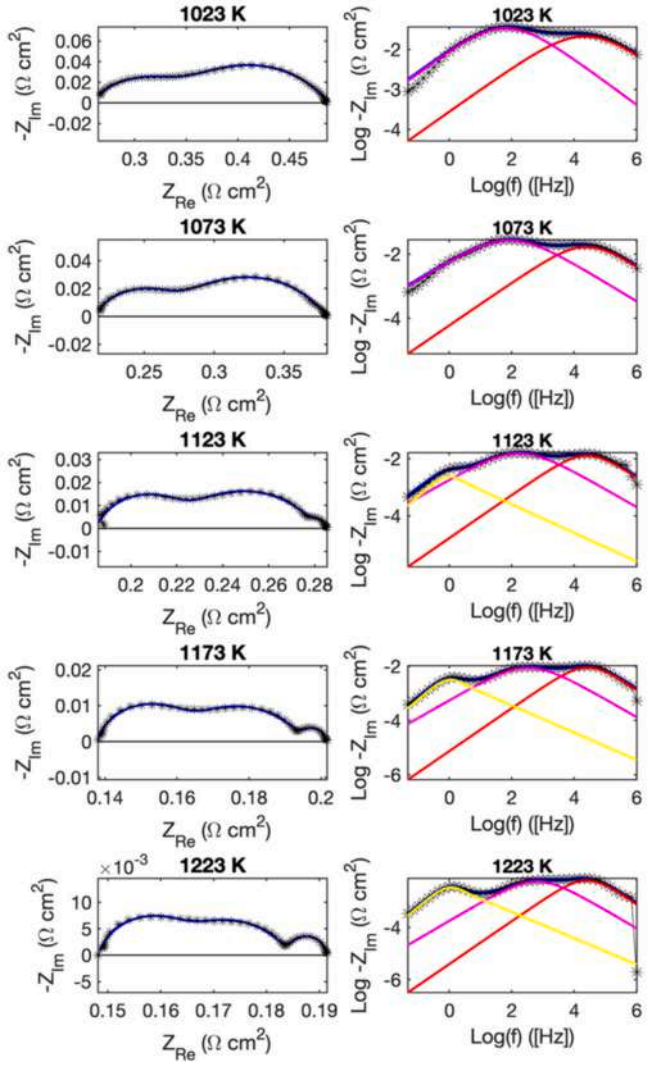

Fig. 16. EIS results obtained from LSCF granular powder cathodes between 1023 K and 1223 K. Symbols: experimental data; blue line: fittings through the Rs-RQ1-RQ2-FLW equivalent circuit. Left: Nyquist plots. Right: Bode plots, also displaying the individual contributions of the RQ1 (red line), RQ2 (magenta line), and FLW (yellow line) circuit elements. (For interpretation of the references to colour in this figure legend, the reader is referred to the web version of this article.)

cm^{-2}, which confirms the attribution to a charge exchange process at the electrode/electrolyte interface [59]. For the EIS spectra of the granular LSCF cathode, EC fitting of the main arc was again performed using the coupled RQ2-G elements. In both granular and nanofiber cathodes, the summit frequency of G element is the same ($f_{max} \sim 10^{0.5}$ Hz at 823 K). The same holds also for the summit frequency of the RQ2 element ($f_{max} \sim 10^{1}$ Hz at 823 K). The equivalent capacitance of the RQ2 element is in the range 1.5×10^{-3} to 1.8×10^{-3} F cm^{-2} for the granular electrode and in the range 2.1×10^{-3} F cm^{-2} to 1.4×10^{-2} F cm^{-2} for the nanofiber electrode. These capacitances are of the same order of magnitude as those reported in the literature for intermediate-frequency processes in LSCF electrodes [57]. The literature attributes these intermediate-frequency processes to interfacial charge transfer [59].

At low temperature (823 K), the impedance of the main EIS middle-frequency arc is approximately the same in both the nanofiber and the granular electrodes, but the relative importance of the contributions associated with the two circuit elements is reversed. Indeed, in the granular electrode, the impedance of the RQ2 element prevails over that of the G element. This may confirm the previously presented idea that the RQ2 impedance is again related to the microstructure of the electrode, and in particular to the charge transfer from one particle to another. In granular electrodes, this may be hindered by the difficult contact and the small number of contact points among different granules.

The results reported above for nanofiber and granular LSCF cathodes are now compared and discussed in more detail with reference to the schemes in Fig. 13. For nanofiber cathodes (Fig. 13 a), the previous observations are consistent with a picture where the fiber/electrolyte and fiber/fiber interfaces are very good, so that RQ1 is not measured and RQ2 is very small. The lack of RQ1 confirms the previous speculations about a very good contact between nanofibers and electrolyte [22], and can be explained considering that fibers lay in-plane over the electrolyte, forming a stable, well-extended, and well-adhering electrode/electrolyte contact. Since the fibers are deposited in-plane, but the net charge transfer is cross-plane, it results that charges have to travel a long path along each fiber (possibly, several μm in length, with a cross-section diameter of around 0.2 μm) before being transferred onto the fiber above (or below) in the 3-D structure (Fig. 13a). This explains why, at low temperature, the G element and the associated impedance (bulk path), are by far the prevailing contributions. By increasing temperature, both the electrochemical reaction and the charge transfer phenomena within the fiber are enhanced exponentially. The Gerischer contribution is expected to benefit from both phenomena, whereas the RQ2 is expected to be associated only with the electrochemical reaction rate. This may explain the reason why the G impedance tends to reduce more quickly than the RQ2 contribution, so that at 1223 K the two contributions become of the same order.

Whereas fibers lay in-plane over the electrolyte, forming a stable and extended electrode/electrolyte contact, in granular electrodes the formation of such a stable interface is problematic, due both to the small number of contact points between the electrode granules and the electrolyte surface, and to the facile modification of the extension of the contact area during the experiment. With reference to the scheme in Fig. 13b, these observations are consistent with a picture of the granular electrode where, due to the difficult granule/granule and granule/electrolyte contact, the RQ1 and RQ2 contributions prevail over the G contribution. The G contribution is rather small, being related to the length of the path along each granule, smaller than in fibers (it is the diameter of one granule, *i.e.* ~ 0.9 μm), and to the larger section area (related again to the granule diameter ~ 0.9 μm). By increasing temperature, impedances associated with all the EC elements decrease, and the G contribution disappears abruptly at ~ 1023 K. This will be further discussed in the following.

4. Discussion

The substantial differences in the electrocatalytic behavior of nanofibers and powders can be harmonically discussed in the light of the structural, microstructural and electrochemical results described in the previous sections. In order to gain a comprehensive view of the whole scenario, the Arrhenius plots deriving from electrochemical data need to be analyzed. R_p^{-1} values deriving from electrochemical data (excluding the low-frequency diffusive arc fitted through the FLW element) for both LSCF nanofibers and granular powders were used to build the Arrhenius plots reported in Fig. 17, which also shows the individual contributions associated with the different EC elements; linear fittings are reported, together with their activation energies.

A comparison with results reported in the literature highlights that LSCF nanofibers data are very reproducible. In particular, the activation energy of 118 kJ/mol reported here for the overall $R_{p,TOT}^{-1}$ (Fig. 17a) is similar to the literature values (for example, 107 kJ/mol in [34]). On the contrary, the literature about LSCF granular electrodes shows a larger variability, with EIS diagrams and activation energies spanning over a wide range. Indeed, the activation energy of the $R_{p,TOT}^{-1}$ (Fig. 17b) for the LSCF granular electrode between 823 K and 973 K is 133 kJ/mol, while

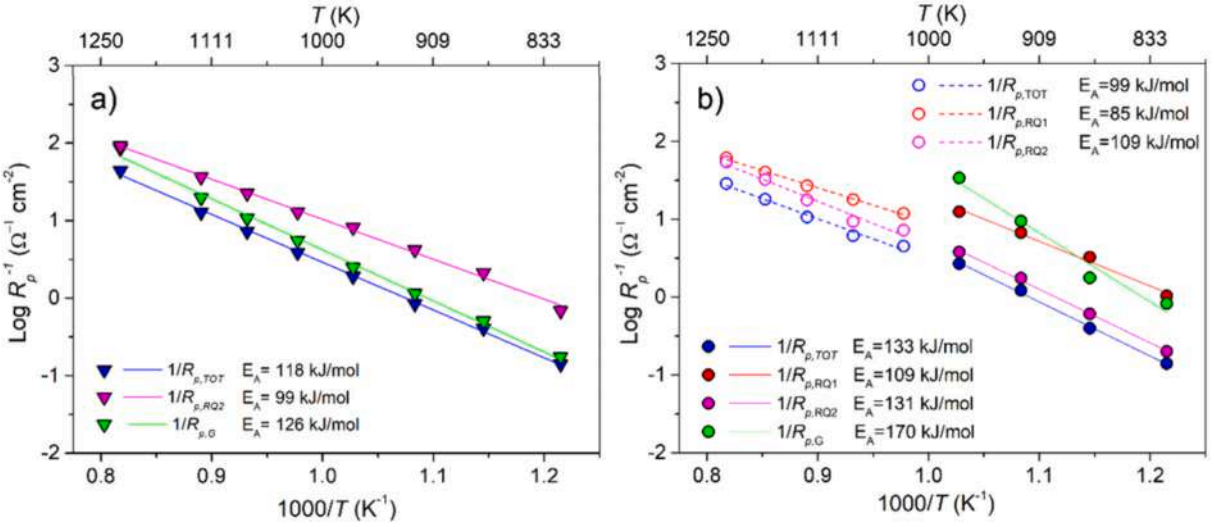

Fig. 17. Arrhenius plot of R_p^{-1} and the individual contributions associated with the different EC elements. The impedance of the FLW element is excluded. Lines are linear fittings, reported together with the associated activation energies. (a) LSCF nanofibers; (b) LSCF granular powders.

literature values vary in the 133–157 kJ/mol range [32,60,61]. This evidence can be explained taking into account that EIS results of granular electrodes are dominated by RQ1 and RQ2, which in this work are considered to be associated with the granule/electrolyte contact and the granule/granule contact respectively. It appears reasonable to assume that the different electrode preparation procedures deeply affect the properties of these interfaces, and therefore the final EIS results. On the contrary, the EIS diagrams of LSCF nanofibers are dominated by the G response, which is associated with the bulk of fibers, characterized by high stability and good reproducibility [32,34,60,61]. Therefore, it can be concluded that the equivalent circuit *Rs – RQ1 – RQ2 – G – FLW* and the related interpretative framework (Fig. 13), applied to the experimental analysis performed in this work, make it possible to propose an explanation for a well known paradox affecting nanofiber and granular LSCF electrodes for IT-SOFC application.

Another aspect worth emphasizing is the striking parallel between the variation with temperature of crystallographic features and electrochemical performance. Interestingly, this parallel takes place with both nanofiber and granular electrodes, despite their markedly different behavior. As previously described, in fact, the crystallographic features of nanofibers gradually vary in the investigated temperature range, whereas granular powders display an abrupt transition around 1023 K, namely where the R → C transition occurs. This behavior is particularly evident for the trends of oxygen occupancy (Fig. 10a), average atomic volume (Fig. 10b), and microstrain ε (Fig. 12). Accordingly, the Arrhenius plots of nanofibers (Fig. 17a) are linear over the whole temperature range, with no slope change, while granular electrodes undergo a clear transition around 1023 K (Fig. 17b). A further remark regards the activation energies: by comparing Fig. 17a and Fig. 17b, it can be observed that at temperatures below 973 K all the activation energies, in particular those of the G and the RQ2 elements, are about 35 kJ/mol larger for granules than for nanofibers. Going back to Fig. 10 and Fig. 12, these show that in the range 773-973 K the variation with temperature of the crystallographic features follows a different trend for LSCF granules and for nanofibers, despite the LSCF having a rhombohedral structure in both cases. Then, Fig. 17 shows that, at temperatures above 1023 K, in granular electrodes, all the activation energies of the electrochemical processes drop dramatically, and this is again in agreement with the discontinuities observed in all the structure-related properties (Figs. 10 and 12). These considerations confirm that there is always a close correlation between the variation with temperature of structural features and electrochemical phenomena. In other words, these observations suggest that the activation energies of all electrochemical processes, including the electrokinetics of the ORR, are not intrinsically and exclusively related to the electrochemical processes themselves, but they incorporate a contribution, possibly of major entity, originating from the variation of crystal structure with temperature.

A point deserving further discussion is the discontinuity occurring in the Arrhenius plot of granular electrodes at the same temperature where the R → C transition takes place, with the aforementioned abrupt decrease in oxygen occupancy (Fig. 17, Fig. 10). The latter effect is expected to boost both the oxygen ion conductivity and the electrochemical reaction in the bulk of the material, which explains why the G element vanishes. On the other hand, data reported in Fig. 17b show that the RQ1 surface path is strongly negatively affected by the R → C transition, showing an abrupt marked drop of $R_{p,RQ1}^{-1}$. This is possibly due to the occurrence of a distortion of the crystal lattice at the interface between the electrolyte and the contacting granules, caused by the R → C transition. A similar effect occurs also with RQ2, although less pronounced. Therefore, the temperature of the R → C transition represents a threshold temperature for LSCF powder electrodes, where the R_p of all the electrochemical processes vary abruptly in strict association with the structural changes occurring. These structural changes are suspected to be associated to lattice distortion at the electrochemically active interfaces, which may trigger degradation. A general conclusion regarding nanofiber LSCF electrodes is that the absence of the R → C transition in the typical operating temperature range of IT-SOFCs can be proposed as one of the reasons for the interesting stability of electrochemical performance demonstrated in previous works [22].

5. Conclusions

Two different LSCF morphologies, namely nanofibers prepared in-house by electrospinning and commercial granular powders used as a control sample, were tested experimentally through synchrotron x-ray diffraction and electrochemical impedance spectroscopy in the 823–1173 K temperature range. The whole study sheds a light on the remarkable differences existing in the structural, microstructural and electrochemical properties of both morphologies, demonstrating that the electrospinning manufacturing process has a significant impact on the features of the perovskite obtained. The crystallographic analysis reveals the occurrence of the rhombohedral (R) to cubic (C) transition at ~ 1023 K in powders, while the R structure is stable over the whole temperature range in nanofibers. In correspondence of the structural

transition, an abrupt discontinuity is also observed in the oxygen occupancy factor and in microstrain. A higher number of oxygen vacancies is found in nanofibers.

The interpretation of the electrochemical impedance spectroscopy results is based on equivalent circuit fitting, through the $Rs - RQ1 - RQ2 - G - FLW$ circuit. This equivalent circuit is demonstrated to provide a general framework for the interpretation of results obtained from both nanofiber and granular LSCF electrodes. Each circuit element is associated to a well-defined physical process. This approach sheds a light on notorious and puzzling behavior of LSCF electrodes, *i.e.* excellent reproducibility of nanofiber electrodes and scarce reproducibility of granular ones. Indeed, the analysis performed suggests that impedance results of nanofiber electrodes are dominated by a Gerischer contribution originating from the bulk of the fibers themselves. Conversely, for granular electrodes the impedance of the granule/electrolyte and granule/granule contacts, whose properties are strongly affected by extrinsic factors related to processing parameters, are prevailing.

While impedance data reveal a single activation energy in nanofibers, it is demonstrated that the temperature of the R → C transition represents a threshold temperature for LSCF powder electrodes, where the R_p and the activation energy of all the electrochemical processes vary abruptly in strict association with the structural changes. As structural transitions may be associated to lattice distortion at the electrochemically active interfaces with consequent degradation, it is recommended to design materials for solid oxide fuel cell electrodes avoiding as much as possible any crystal structure transition in the operating range. Nanofiber electrodes offer higher guarantees in this respect since the R → C transition temperature is above the operating range of IT-SOFCs. The absence of the R → C transition in the typical operating temperature range of IT-SOFCs can therefore be proposed as one of the reasons for the interesting stability of electrochemical performance demonstrated in previous works.

The results presented emphasize a striking parallelism between the variation with temperature of crystallographic features and electrochemical performance for both nanofiber and granular electrodes, thus suggesting that the activation energies of all electrochemical processes, including the electrokinetics of the ORR, incorporate a contribution originating from the variation with temperature of crystal structure and associated properties, in particular oxygen occupancy.

In conclusion, this investigation provides new insights into the influence of the electrospinning synthesis route on the crystalline properties of LSCF materials and highlights the impact of these structural characteristics on the electrocatalytic activity in SOFCs. Specifically, the persistence of the rhombohedral structure in electrospun nanofibers up to higher temperatures suggests potential advantages in terms of stability and electrochemical performance over granular powders, which experience a structural transition that affects their electrochemical properties. This research opens new pathways for the design and development of high-performance materials for IT-SOFC applications, emphasizing the critical role of synthesis methods in determining the functional properties of electrode materials.

CRediT authorship contribution statement

Marta Daga: Writing – original draft, Investigation, Formal analysis. **Caterina Sanna:** Investigation, Formal analysis. **Giorgio Bais:** Investigation. **Maurizio Polentarutti:** Investigation. **Sara Massardo:** Investigation, Formal analysis. **Marilena Carnasciali:** Formal analysis. **Peter Holtappels:** Formal analysis. **Paola Costamagna:** Writing – review & editing, Methodology, Conceptualization. **Marcella Pani:** Writing – review & editing, Supervision, Resources, Methodology, Funding acquisition, Conceptualization. **Cristina Artini:** Writing – review & editing, Conceptualization.

Declaration of competing interest

The authors declare that they have no known competing financial interests or personal relationships that could have appeared to influence the work reported in this paper.

Data availability

Data will be made available on request.

Acknowledgments

The group at the University of Genoa, Italy, acknowledges financial support from the San Paolo Project 'COELUS - Production of renewable fuel by CO-ELectrolysis and reUSe of carbon dioxide' (ID ROL 32604). The Elettra synchrotron facility is kindly acknowledged for the provision of beamtime (proposal number: 20195219). Marie Lund Traulsen and Wenjing Zhang are acknowledged for their contribution to the electrochemical tests carried out at the Technical University of Denmark.

References

[1] I. Riess, Mixed ionic-electronic conductors - material properties and applications, Solid State Ionics 157 (2003) 1–17, https://doi.org/10.1016/S0167-2738(02)00182-0.
[2] M. Hanif, S. Rauf, M. Motola, Z. Babar, C.-J. Li, C.-X. Li, Recent progress of perovskite-based electrolyte materials for solid oxide fuel cells and performance optimizing strategies for energy storage applications, Mater. Res. Bull. 146 (2021) 111612, https://doi.org/10.1016/j.materresbull.2021.111612.
[3] F. Lu, T. Xia, Q. Li, J. Wang, L. Huo, H. Zhao, Heterostructured simple perovskite nanrod-decorated double perovskite cathode for solid oxide fuel cells: highly catalytic activity, stability and CO_2-durability for oxygen reduction reaction, Appl. Catal. B Environ. 249 (2019) 19–31, https://doi.org/10.1016/j.apcatb.2019.02.056.
[4] S. Pang, J. Xu, Y. Su, G. Yang, M. Zhu, M. Cui, X. Shen, C. Chen, The role of A-site cation size mismatch in tune the catalytic activity and durability of double perovskite oxides, Appl. Catal. B Environ. 270 (2020) 118868, https://doi.org/10.1016/j.apcatb.2020.118868.
[5] S. Jo, H.G. Jeong, Y.H. Kim, D. Neagu, J.-H. Myung, Stability and activity controls of Cu nanoparticles for high-performance solid oxide fuel cells, Appl. Catal. B Environ. 285 (2021) 119828, https://doi.org/10.1016/j.apcatb.2020.119828.
[6] N. Mushtaq, Y. Lu, C. Xia, W. Dong, B. Wang, M.A.K.Y. Shah, S. Rauf, M. Akbar, E. Hu, R. Raza, M.I. Asghar, P.D. Lund, Promoted electrocatalytic activity and ionic transport simultaneously in dual functional Ba0.5Sr0.5Fe0.8Sb0.2O3-δ-Sm0.2Ce0.8O2-δ heterostructure, Appl. Catal. B Environ. 298 (2021) 120503, https://doi.org/10.1016/j.apcatb.2021.120503.
[7] M. Qin, Y. Xiao, H. Yang, T. Tan, Z. Wang, X. Fan, C. Yang, Ru/Nb co-doped perovskite anode: achieving good coking resistance in hydrocarbon fuels via core-shell nanocatalysts exsolution, Appl. Catal. B Environ. 299 (2021) 120613, https://doi.org/10.1016/j.apcatb.2021.120613.
[8] S.P. Jiang, Development of lanthanum strontium cobalt ferrite perovskite electrodes of solid oxide fuel cells – a review, Int. J. Hydr. En. 44 (2019) 7448–7493, https://doi.org/10.1016/j.ijhydene.2019.01.212.
[9] C. Artini, Crystal chemistry, stability and properties of interlanthanide perovskites: a review, J. Eur. Ceram. Soc. 37 (2017) 427–440, https://doi.org/10.1016/j.jeurceramsoc.2016.08.041.
[10] A.M. Glazer, The classification of tilted octahedra in perovskites, Acta Cryst. B. 28 (1972) 3384–3392, https://doi.org/10.1107/S0567740872007976.
[11] K.S. Aleksandrov, Successive structural phase transitions in perovskites. 1. Symmetry of distorted phases, Kristallografiya 21 (1976) 249–255.
[12] L.-.W. Tai, M.M. Nasrallah, H.U. Anderson, D.M. Sparlin, S.R. Sehlin, Structure and electrical properties of $La_{1-x}Sr_xCo_{1-y}Fe_yO_3$. Part 2. The system $La_{1-x}Sr_xCo_{0.2}Fe_{0.8}O_3$, Solid State Ionics 76 (1994) 273–283, https://doi.org/10.1016/0167-2738(94)00245-N.
[13] B.X. Huang, J. Malzbender, R.W. Steinbrech, L. Singheiser, Mechanical properties of $La_{0.58}Sr_{0.4}Co_{0.2}Fe_{0.8}O_{3-\delta}$ membranes, Solid State Ionics 180 (2009) 241–245, https://doi.org/10.1016/j.ssi.2008.11.005.
[14] S. Wang, M. Katsuki, M. Dokiya, T. Hashimoto, High temperature properties of $La_{0.6}Sr_{0.4}Co_{0.8}Fe_{0.2}O_{3-\delta}$ phase structure and electrical conductivity, Solid State Ionics 159 (2003) 71–78, https://doi.org/10.1016/S0167-2738(03)00027-4.
[15] P.T. Geiger, N.H. Khansur, K. Riess, A. Martin, M. Hinterstein, K.G. Webber, Stress-dependent crystal structure of lanthanum strontium cobalt ferrite by in situ synchrotron X-ray diffraction, J. Appl. Phys. 123 (2018) 075104, https://doi.org/10.1063/1.5017934.
[16] A. Fossdal, M. Menon, I. Wærnhus, K. Wiik, M. Einarsrud, T. Grand, Crystal structure and thermal expansion of $La_{1-x}Sr_xFeO_{3-\delta}$ materials, J. Am. Ceram. Soc. 87 (2004) 1952–1958, https://doi.org/10.1111/j.1151-2916.2004.tb06346.x.
[17] M. Katsuki, S. Wang, M. Dokiya, T. Hashimoto, High temperature properties of $La_{0.6}Sr_{0.4}Co_{0.8}Fe_{0.2}O_{3-\delta}$ oxygen nonstoichiometry and chemical diffusion constant,

Solid State Ionics 156 (2003) 453–461, https://doi.org/10.1016/S0167-2738(02)00733-6.
[18] L. Spiridigliozzi, E. Di Bartolomeo, G. Dell'Agli, F. Zurlo, GDC-based infiltrated electrodes for solid oxide electrolyzer cells (SOECs), Appl. Sci. 10 (2020) 3882, https://doi.org/10.3390/app10113882.
[19] M. Sha, S.A. Barnett, Solid oxide fuel cell cathodes by infiltration of $La_{0.6}Sr_{0.4}Co_{0.2}Fe_{0.8}O_{3-\delta}$ into Gd-doped ceria, Solid State Ionics 179 (2008) 2059–2064, https://doi.org/10.1016/j.ssi.2008.07.002.
[20] S. Lee, H.W. Song, S.H. Hyun, J. Kim, J. Moon, LSCF–SDC core–shell high-performance durable composite cathode, J. Power Sources 195 (2010) 118–123, https://doi.org/10.1016/j.jpowsour.2009.06.079.
[21] C. Sanna, W. Zhang, P. Costamagna, P. Holtappels, Synthesis and electrochemical characterization of $La_{0.6}Sr_{0.4}Co_{0.2}Fe_{0.8}O_{3-\delta}$ /$Ce_{0.9}Gd_{0.1}O_{1.95}$ co-electrospun nanofiber cathodes for intermediate-temperature solid oxide fuel cells, Int. J. Hydr. En. 46 (2021) 13818–13831, https://doi.org/10.1016/j.ijhydene.2020.11.216.
[22] A. Enrico, W. Zhang, M. Lund Traulsen, E.M. Sala, P. Costamagna, P. Holtappels, $La_{0.6}Sr_{0.4}Co_{0.2}Fe_{0.8}O_{3-\delta}$ nanofiber cathode for intermediate-temperature solid oxide fuel cells by water-based sol-gel electrospinning: synthesis and electrochemical behaviour, J. Eur. Ceram. Soc. 38 (2018) 2677–2686, https://doi.org/10.1016/j.jeurceramsoc.2018.01.034.
[23] P. Costamagna, P. Holtappels, C. Sanna, Metal Oxide Nanofiber-Based Electrodes in Solid Oxide Fuel Cells, Chapter 13 in Metal Oxide-Based Nanofibers and Their Applications, 2022, pp. 301–331. Elsevier, Amsterdam, https://doi.org/10.1016/B978-0-12-820629-4.00013-8.
[24] A. Enrico, B. Aliakbarian, A. Lagazzo, A. Donazzi, R. Botter, P. Perego, P. Costamagna, Parameter optimization for the electrospinning of $La_{1-x}Sr_xCo_{1-y}Fe_yO_{3-\delta}$ fibers for IT-SOFC electrodes, Fuel Cells 17 (2017) 415–422, https://doi.org/10.1002/fuce.201600190.
[25] A. Greiner, J.H. Wendorff, Electrospinning: a fascinating method for the preparation of ultrathin fibers, Angew. Chem. Int. Ed. 46 (2007) 5670–5703, https://doi.org/10.1002/anie.200604646.
[26] N. Bhardwaj, S.C. Kundu, Electrospinning: a fascinating fiber fabrication technique, Biotechnol. Adv. 28 (2010) 325–347, https://doi.org/10.1016/j.biotechadv.2010.01.004.
[27] W.E. Teo, S. Ramakrishna, A review on electrospinning design and nanofibre assemblies, Nanotechnology 17 (2006) 89–106, https://doi.org/10.1088/0957-4484/17/14/R01.
[28] J. Parbey, Q. Wang, J. Lei, M. Espinoza-Andaluz, F. Hao, Y. Xiang, T. Li, M. Andersson, High-performance solid oxide fuel cells with fiber-based cathodes for low-temperature operation, Int. J. Hydr. En. 45 (2020) 6949–6957, https://doi.org/10.1016/j.ijhydene.2019.12.125.
[29] M.E. Orazem, B. Tribollet, Electrochemical Impedance Spectroscopy, John Wiley & Sons, Hoboken, 2008.
[30] J. Nielsen, T. Jacobsen, M. Wandel, Impedance of porous IT-SOFC LSCF:CGO composite cathodes, Electrochim. Acta 56 (2011) 7963–7974, https://doi.org/10.1016/j.electacta.2011.05.042.
[31] P. Costamagna, E.M. Sala, W. Zhang, M. Lund Traulsen, P., Holtappels, electrochemical impedance spectroscopy of $La_{0.6}Sr_{0.4}Co_{0.2}Fe_{0.8}O_{3-\delta}$ nanofiber cathodes for intermediate temperature-solid oxide fuel cell applications: a case study for the 'depressed' or 'fractal' Gerischer element, Electrochim. Acta 319 (2019) 657–671, https://doi.org/10.1016/j.electacta.2019.06.068.
[32] A. Esquirol, N.P. Brandon, J.A. Kilner, M. Mogensen, Electrochemical characterization of La0.6Sr0.4Co0.2Fe0.8O3 cathodes for intermediate-temperature SOFCs, J. Electrochem. Soc. 151 (2004) A1847–A1855, https://doi.org/10.1149/1.1799391.
[33] M. Lubini, E. Chinarro, B. Moreno, V.C. de Sousa, A.K. Alves, C.P. Bergmann, Electrical properties of $La_{0.6}Sr_{0.4}Co_{1-y}Fe_yO_3$ (y = 0.2−1.0) fibers obtained by electrospinning, J. Phys. Chem. C 120 (2016) 64–69, https://doi.org/10.1021/acs.jpcc.5b09696.
[34] Y. Chen, Y. Bu, Y. Zhang, R. Yan, D. Ding, B. Zhao, S. Yoo, D. Dang, R. Hu, C. Yang, M. Liu, Highly efficient and robust nanofiber cathode for solid oxide fuel cells, Adv. Energy Mater. 7 (2017) 1601890, https://doi.org/10.1002/aenm.201601890.
[35] P. Costamagna, C. Sanna, A. Campodonico, E.M. Sala, R. Saẑinas, P. Holtappels, Electrochemical impedance spectroscopy of electrospun $La_{0.6}Sr_{0.4}Co_{0.2}Fe_{0.8}O_3$ ed nanorod cathodes for intermediate temperature e solid oxide fuel cells, Fuel Cells 19 (2019) 472–483, https://doi.org/10.1002/fuce.201800205.
[36] J. Schindelin, I. Arganda-Carreras, E. Frise, V. Kaynig, M. Longair, T. Pietzsch, S. Preibisch, C. Rueden, S. Saalfeld, B. Schmid, J.-Y. Tinevez, D.J. White, V. Hartenstein, K. Eliceiri, P. Tomancak, A. Cardona, Fiji: an open-source platform for biological-image analysis, Nat. Methods 9 (2012) 676, https://doi.org/10.1038/nmeth.2019.
[37] A.P. Hammersley, FIT2D: a multi-purpose data reduction, analysis and visualization program, J. Appl. Crystallogr. 49 (2016) 646–652, https://doi.org/10.1107/S1600576716000455.
[38] J. Rodriguez-Carvajal, Recent advances in magnetic structure determination by neutron powder diffraction, Phys. B Condens. Matter 192 (1993) 55–69, https://doi.org/10.1016/0921-4526(93)90108-I.
[39] R.T. Roisnel, J. Rodriguez-Carvajal, A windows tool for powder diffraction patterns analysis, Mater. Sci. Forum 378-381 (2000) 118–123, https://doi.org/10.4028/www.scientific.net/MSF.378-381.118.
[40] T. Itoh, M. Nakayama, Using in situ X-ray absorption spectroscopy to study the local structure and oxygen ion conduction mechanism in $(La_{0.6}Sr_{0.4})(Co_{0.2}Fe_{0.8})O_{3-d}$, J. Solid State Chem. 192 (2012) 38–46, https://doi.org/10.1016/j.jssc.2012.03.021.
[41] J. Dailly, S. Fourcade, A. Largeteau, F. Mauvy, J.C. Grenier, M. Marrony, Perovskite and A_2MO_4-type oxides as new cathode materials for protonic solid oxide fuel cells, Electrochim. Acta 55 (2010) 5847–5853, https://doi.org/10.1016/j.electacta.2010.05.034.
[42] G. Bergerhoff, M. Berndt, K. Brandenburg, T. Degen, Concerning inorganic crystal structure types, Acta Crystallogr. B55 (1999) 147–156, https://doi.org/10.1107/S0108768198010969.
[43] H.M. Rietveld, A profile refinement method for nuclear and magnetic structures, J. Appl. Crystallogr. 2 (1969) 65–71, https://doi.org/10.1107/S0021889869006558.
[44] A. Weber, E. Ivers-Tiffée, Materials and concepts for solid oxide fuel cells (SOFCs) in stationary and mobile applications, J. Power Sources 127 (2004) 273–283, https://doi.org/10.1016/j.jpowsour.2003.09.024.
[45] A.J. Jacobson, Materials for solid oxide fuel cells, Chem. Mater. 22 (2010) 660–674, https://doi.org/10.1021/cm902640j.
[46] C. Artini, M. Pani, A. Lausi, R. Masini, G.A. Costa, High temperature structural study of Gd-doped ceria by synchrotron X-ray diffraction (673 K ≤ T ≤ 1073 K), Inorg. Chem. 53 (2014) 10140–10149.
[47] M. Brisotto, F. Cernuschi, F. Drago, C. Lenardi, P. Rosa, C. Meneghini, M. Merlini, C. Rinaldi, High temperature stability of Ba0.5Sr0.5Co0.8Fe0.2O3−1 and La0.6Sr0.4Co1−yFeyO3−1 oxygen separation perovskite membranes, J. Eur. Ceram. Soc. 36 (2016) 1679–1690, https://doi.org/10.1016/j.jeurceramsoc.2016.01.029.
[48] E. Effori, J. Laurencin, E. Da Rosa Silva, M. Hubert, T. David, M. Petitjean, G. Geneste, L. Dessemond, E. Siebert, An elementary kinetic model for the LSCF and LSCF-CGO electrodes of solid oxide cells: impact of operating conditions and degradation on the electrode response, J. Electrochem. Soc. 168 (2021) 044520, https://doi.org/10.1149/1945-7111/abf40a.
[49] W.H. Hall, X-ray line broadening in metals, Proc. Phys. Soc. Sect. A. 62 (1949) 741–743, https://doi.org/10.1088/0370-1298/62/11/110.
[50] G.K. Williamson, W.H. Hall, X -ray line broadening from filed aluminium and wolfram, Acta Metall. 1 (1953) 22–31, https://doi.org/10.1016/0001-6160(53)90006-6.
[51] C. Artini, M. Viviani, S. Presto, S. Massardo, M.M. Carnasciali, L. Gigli, M. Pani, Correlations between structure, microstructure and ionic conductivity in (Gd,Sm)-doped ceria, Phys. Chem. Chem. Phys. 24 (2022) 23622–23633, https://doi.org/10.1039/d2cp03255d.
[52] H. Gerischer, Echselstrompolarisation von Elektrodenmit einem potential-bestimmenden Schritt beim Gleichgewichtspotential. I, Z. Phys. Chem. 198 (1951) 286–313.
[53] S.B. Adler, Factors governing oxygen reduction in solid oxide fuel cell cathodes, Chem. Rev. 104 (2004) 4791–4843, https://doi.org/10.1021/cr020724o.
[54] B.A. Boukamp, A nonlinear least squares fit procedure for analysis of immittance data of electrochemical systems, Solid State Ionics 20 (1986) 31–44, https://doi.org/10.1016/0167-2738(86)90031-7.
[55] M.S. Harding, B. Tribollet, V. Vivier, M.E. Orazem, The influence of homogeneous reactions on the impedance response of a rotating disk electrode, J. Electrochem. Soc. 164 (2017) E3418–E3428, https://doi.org/10.1149/2.0411711jes.
[56] S. Koch, K.V. Hansen, B.S. Johansen, Elchemea. https://www.elchemea.dk, 2005 (Last accessed 26 April 2024).
[57] V.C. Kournoutis, F. Tietz, S. Bebelis, AC impedance characterisation of a $La_{0.8}Sr_{0.2}Co_{0.2}Fe_{0.8}O_{3-\delta}$ electrode, Fuel Cells 9 (2009) 852–860, https://doi.org/10.1002/fuce.200800120.
[58] M.J. Jørgensen, M. Mogensen, Impedance of solid oxide fuel cell LSM/YSZ composite cathodes, J. Electrochem. Soc. 148 (2001) A433–A442, https://doi.org/10.1149/1.1360203.
[59] L. Fan, P.-C. Su, Layer-structured LiNi0.8Co0.2O2: a new triple (H+/O2−/e-) conducting cathode for low temperature proton conducting solid oxide fuel cells, J. Power Sources 306 (2016) 369–377, https://doi.org/10.1016/j.jpowsour.2015.12.015.
[60] J. Chen, F. Liang, B. Chi, J. Pu, S.P. Jiang, L. Jian, Palladium and ceria infiltrated La0.8Sr0.2Co0.5Fe0.5O3-δ cathodes of solid oxide fuel cells, J. Power Sources 194 (2009) 275–280, https://doi.org/10.1016/j.jpowsour.2009.04.041.
[61] H.J. Hwang, J.-W. Moon, S. Lee, E.A. Lee, Electrochemical performance of LSCF-based composite cathodes for intermediate temperature SOFCs, J. Power Sources 145 (2005) 243–248, https://doi.org/10.1016/j.jpowsour.2005.02.063.